Water Research 185 (2020) 116195

Contents lists available at ScienceDirect

Water Research

journal homepage: www.elsevier.com/locate/watres

Process-based modeling of arsenic(III) oxidation by manganese oxides under circumneutral pH conditions

Bhasker Rathi[a,b,c], James Jamieson[b,c], Jing Sun[d,b,c,*], Adam J. Siade[b,c,e], Mengqiang Zhu[f], Olaf A. Cirpka[a], Henning Prommer[b,c,e,*]

[a] Center for Applied Geoscience, University of Tübingen, Tübingen, Germany
[b] School of Earth Sciences, University of Western Australia, Crawley WA 6009, Australia
[c] CSIRO Land and Water, Private Bag No. 5, Wembley WA 6913, Australia
[d] State Key Laboratory of Environmental Geochemistry, Institute of Geochemistry, Chinese Academy of Sciences, Guiyang 550081, China
[e] National Centre for Groundwater Research and Training (NCGRT), Australia
[f] Department of Ecosystem Science and Management, University of Wyoming, Laramie WY 82071 United States

ARTICLE INFO

Article history:
Received 13 May 2020
Revised 5 July 2020
Accepted 16 July 2020
Available online 17 July 2020

Keywords:
Manganese oxide
Arsenic
Process-based modeling
Surface complexation model
Edge sites
Surface passivation

ABSTRACT

Numerous experimental studies have identified a multi-step reaction mechanism to control arsenite (As(III)) oxidation by manganese (Mn) oxides. The studies highlighted the importance of edge sites and intermediate processes, e.g., surface passivation by reaction products. However, the identified reaction mechanism and controlling factors have rarely been evaluated in a quantitative context. In this study, a process-based modeling framework was developed to delineate and quantify the relative contributions and rates of the different processes affecting As(III) oxidation by Mn oxides. The model development and parameterization were constrained by experimental observations from literature studies involving environmentally relevant Mn oxides at circumneutral pH using both batch and stirred-flow reactors. Our modeling results highlight the importance of a transitional phase, solely evident in the stirred-flow experiments, where As(III) oxidation gradually shifts from fast reacting Mn(IV) to slowly reacting Mn(III) edge sites. The relative abundance of these edge sites was the most important factor controlling the oxidation rate, whereas surface passivation restricted oxidation only in the stirred-flow experiment. The Mn(III) edge sites were demonstrated to play a crucial role in the oxidation and therefore in controlling the long-term fate of As. This study provided an improved understanding of Mn oxide reactivity and the significance in the cycling of redox-sensitive metal(loid)s in the environment.

1. Introduction

Manganese (Mn) oxides play a key role in the cycling of redox-sensitive metal(loid)s in the environment due to their high redox potential and ubiquitous presence in soils and sediments (Jenne, 1968; Post, 1999; Yao and Millero, 1996). Mn oxides are also preferred for their strong adsorption and oxidizing properties in treatment of wastewater effluent containing heavy metal ions, dyes, pesticides, leachates, oil spills and pharmaceuticals (De Rudder et al., 2004; Du et al., 2020; Husnain et al., 2020; Song et al., 2019). Their effect on arsenic (As) cycling has been studied extensively in both natural environments (Takamatsu et al., 1985) and water treatment (Driehaus et al., 1995; Gude et al., 2017) because of the health threat that As contaminated groundwater poses globally (Fendorf et al., 2010; Smedley and Kinniburgh, 2002). Perhaps the most relevant impact on As cycling occurs when Mn oxides oxidize the more toxic, and arguably more mobile, arsenite (As(III)) to arsenate (As(V)) (Bai et al., 2016; Huling et al., 2017; Smedley and Kinniburgh, 2002; Tamaki and Frankenberger, 1992). The oxidation is known to follow a multi-step mechanism which involves complex interactions of As(III) with the surface of Mn oxides via adsorption/desorption and surface-bound oxidation (Manning et al., 2002; Nesbitt et al., 1998; Scott and Morgan, 1995; Tournassat et al., 2002).

Mn oxides of different structure and/or particle size have variable reactivity towards As(III) oxidation (Schacht and Ginder-Vogel, 2018). Both layered and tunneled structures are common Mn oxides in the environment; however, the layered structures are much more abundant than the tunneled ones in most environments, probably due to enhanced stability of the former by adsorption of divalent metal cations (Yang et al., 2019). Furthermore,

* Corresponding authors.
E-mail addresses: sunjing@mail.gyig.ac.cn (J. Sun), henning.prommer@csiro.au (H. Prommer).

https://doi.org/10.1016/j.watres.2020.116195
0043-1354/

structural defects are common in layered Mn oxides and contribute to distinct mineral properties. Specifically, Mn(III) substitutions in the mineral lattice affect the average Mn oxidation number (AMON) while Mn vacancies in the layer serve as vacancy sorption sites which have strong affinity for adsorption of metal ions. Variations in particle sizes control the specific surface area (SSA) and affect the number of edge sites that are also important adsorption sites. Although the point of zero charge (PZC) of Mn oxides is generally low, the PZC of edge sites is expected to be higher than that of vacancy sites (Peacock and Sherman, 2007; Tonkin et al., 2004; Villalobos, 2015). Thus, under most environmentally-relevant pH conditions, vacancy sites carry a highly negative charge while the edge sites have a variable charge, depending on the pH and the oxidation state of Mn (Mn(III) versus Mn(IV)). As a result, while Mn^{2+} can adsorb on both edge and vacancy sites (Wang et al., 2019), As(III) and As(V) oxyanions adsorb only on the edge sites (Tournassat et al., 2002). Furthermore, Mn(IV) is considered to adsorb and oxidize As(III) more strongly than Mn(III) and, therefore, an increasing extent of Mn(III) substitutions can reduce Mn oxide oxidative reactivity. This behavior is also observed for uranium (Wang et al., 2013) but is in contrast to the importance of Mn(III) availability in oxidation of chromium and phenolic compounds (Hu et al., 2019; Qian et al., 2019; Nico and Zasoski, 2000). Accordingly, layered Mn(IV) oxides with a high edge-site density and a low fraction of Mn(III) substitutions are most reactive towards As(III) oxidation.

One of the suggested oxidation pathways (Lafferty et al., 2010a,b) involves As(III) being adsorbed on the edge sites via a double-corner sharing, also known as bidentate-binuclear surface complex (Zhu et al., 2009), and then oxidized to As(V), thereby producing intermediate Mn(III) edge sites. Subsequent adsorption and oxidation of As(III) on the Mn(III) edge sites produces As(V) and Mn(II) (Lafferty et al., 2010a; Manning et al., 2002; Nesbitt et al., 1998; Scott and Morgan, 1995; Zhu et al., 2009) while simultaneously exposing *new* Mn(IV) edge sites, thereby allowing the oxidation to proceed further (Scott and Morgan, 1995). Meanwhile, the reaction products As(V) and Mn(II) may suppress the accessibility of the edge sites to As(III), a process known as surface passivation. This may occur through competitive sorption and/or by formation of Mn(II)-As(V) precipitates or ternary surface complexes (Tournassat et al., 2002; Zhu et al., 2009). An alternate oxidation pathway has also been suggested (Lafferty et al., 2010a, 2010b), which involves an additional process known as comproportionation to produce surface Mn(III) from oxidation of adsorbed Mn(II) by Mn(IV) on either edge or vacancy sites (Lafferty et al., 2010b; Wang et al., 2019, 2018; Zhao et al., 2016).

Although many aspects of the multi-step reaction mechanism have been discussed in the literature, we still have only a rudimentary understanding of the As(III) oxidation kinetics and how they are influenced by the inter-relationships between the various reaction steps. For instance, changes to the abundance of initially present Mn(IV) and intermediately formed Mn(III) sites and their effect on As(III) oxidation rate are vastly unknown. The extent and contributing species of surface passivation is also ill-defined. At certain pH values, edge sites may become unavailable for As(III) adsorption or favor adsorption of competing solutes, thus enhancing surface passivation effects. Until now the effects of pH on As(III) oxidation rates have never been quantified.

Many previous studies (Rathi et al., 2017a; Stollenwerk et al., 2007; Wallis et al., 2010; Ying et al., 2011) that quantified oxidation rates lumped all steps into a single stoichiometric reaction (Oscarson et al., 1980) that follows a first-order rate law with respect to As(III) concentration in solution:

$$MnO_2(s) + H_3AsO_3 + H^+ \rightarrow Mn^{2+} + H_2AsO_4^- + H_2O \quad (1)$$

$$r_{As(III)} = \frac{\partial As(III)}{\partial t} = -k_{obs} \times [H_3AsO_3] \quad (2)$$

However, given the complexity of the mechanism, the often strong temporal variations of the rates and the varying factors that can be rate-controlling under changing geochemical conditions, it is not surprising that the values of the reported empirical rate constant (k_{obs}) range over several orders of magnitude among different studies even when they were all conducted with batch reactors (Schacht and Ginder-Vogel, 2018). Empirical models, while sometimes useful, are generally unable to provide mechanistic insights to the reaction mechanism and apart from a few exceptions (Amirbahman et al., 2006; Feng et al., 2018), no attempts have been made to develop more comprehensive models. In contrast to empirical models, process-based models are substantially better equipped to support the identification and delineation of the various interdependent factors that may affect the fate of As(III) during its oxidation by Mn oxides (Schacht and Ginder-Vogel, 2018), such as, As(III) adsorption/desorption and oxidation on Mn oxide surface sites, reactivity of different types of Mn oxides, pH and the role of competitive solutes. To adequately quantify adsorption/desorption reactions, surface complexation models (SCMs) have proven to be a powerful tool to integrate information on mineral surface areas, sorption site densities, and surface-charge effects with respect to pH while also considering the impacts from different competing species (Davis and Kent, 1990; Liu et al., 2019). However, at present the challenge of developing SCMs that describe the adsorption/desorption of As(III), As(V) and Mn(II) on edge and vacancy sites of Mn oxides is that most of the parameters, including the required surface complexation constants, are not readily available in the literature. Selecting appropriate experimental data from the literature and calibrating the numerical model against those data using suitable optimization methods can help derive these valuable parameters. The end result will be a quantitative framework which elucidates the reaction mechanism and can be used to analyze future experiments and to further evaluate the proposed reaction mechanism (Prommer et al., 2019).

The main objective of this study therefore was (i) to develop a process-based, data-constrained framework to assess the adequacy of a conceptual model describing As(III) oxidation by layered Mn oxides; and (ii) to quantitatively evaluate the role of edge sites and surface passivation on the oxidation rate under circumneutral pH conditions. In this study, we focus on the analysis of laboratory experiments from the literature that were conducted over an extended duration and with synthetic layered Mn oxides, which are considered a suitable analog to natural Mn oxides, and at pH values most relevant to natural groundwater systems (Lafferty et al., 2011, 2010a; Villalobos et al., 2014).

2. Materials and method

2.1. Modeling approach and procedure

The modeling procedure started with the development of a conceptual model that, based on our survey of the current literature, incorporates the potentially relevant details of the reaction mechanism (Fig. 1). Subsequently, the assembled conceptual model was evaluated against the most suitable literature datasets. This was achieved by translating the conceptual model of the reaction processes into a numerical model and by comparing the simulated concentrations with the corresponding experimental observations. The numerical implementation required (i) the spatial and temporal discretization of the considered lab experiments, (ii) the definition of an adequate reaction network consisting of a mixture of equilibrium and kinetically controlled geochemical reactions and (iii) a calibration of adjustable model parameters in conjunction with a successive refinement of the proposed conceptual model.

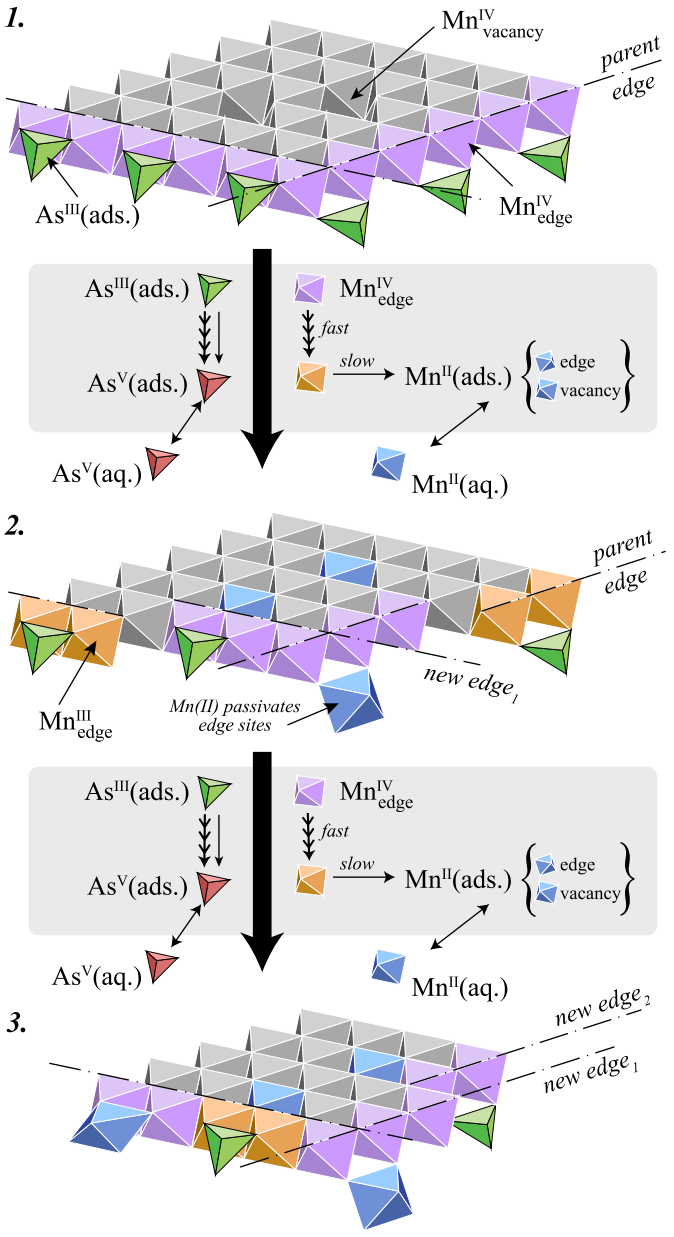

Fig. 1. Schematic illustration of the adopted conceptual model for As(III) oxidation by Mn oxides.

2.2. Conceptual model and numerical implementation

To isolate the specific role of Mn oxide edge surfaces for As(III) oxidation, we separated the total concentration of Mn oxide into edge (C_{edge}) and bulk (C_{bulk}) components. Accordingly, the edge (both $\equiv Mn^{IV}_{edge}$ and $\equiv Mn^{III}_{edge}$) and the vacancy ($\equiv Mn^{IV}_{vacancy}$) sites are stoichiometrically linked with the temporally varying concentrations of C_{edge} and C_{bulk}, respectively.

In this study, we focus on one of the suggested oxidation pathways in which As(III) is adsorbed on the edge sites via bidentate-binuclear surface complexation (Tables 1 and 2). Once adsorbed, As(III) is oxidized to As(V) on $\equiv Mn^{IV}_{edge}$ sites at the rate defined as:

$$r_1 = \frac{\partial As(III)}{\partial t} = -k_1 \times \left[\left(\equiv Mn^{IV}_{edge} - O\right)_2 As^{III}OH\right] \quad (3)$$

Simultaneously, the $\equiv Mn^{IV}_{edge}$ sites are transformed into $\equiv Mn^{III}_{edge}$ sites, where As(III) also adsorbs and is oxidized at the rate:

$$r_2 = \frac{\partial As(III)}{\partial t} = -k_2 \times \left[\left(\equiv Mn^{III}_{edge} - O\right)_2 As^{III}OH\right] \quad (4)$$

where k_1 and k_2 are the first-order rate constant (s^{-1}), and $[(\equiv Mn^{IV}_{edge} - O)_2 As^{III}OH]$ and $[(\equiv Mn^{III}_{edge} - O)_2 As^{III}OH]$ are adsorbed concentrations of As(III) on Mn(IV) and Mn(III) edge sites (mol L^{-1}), respectively. Adsorbed As(III) concentrations are quantified through a SCM, which incorporates the effects of Mn oxide mineral reactivity, solution pH, aqueous As(III) speciation and competitive sorption by other solutes.

Coupled to the oxidation, the reductive dissolution of Mn oxides occurs on the mineral edge, where $\equiv Mn^{III}_{edge}$ sites are reduced to aqueous Mn(II) and cause C_{edge} to decrease. This step also triggers the exposure of a *new* edge surface on C_{bulk} that hosts *new* $\equiv Mn^{IV}_{edge}$ sites (Fig. 1). This was numerically implemented by transferring the corresponding amounts of Mn oxide from C_{bulk} to C_{edge} at a rate proportional to the rate of As(III) oxidation that occurs on the $\equiv Mn^{III}_{edge}$ sites (Eq. (4)):

$$\frac{\partial C_{bulk}}{\partial t} = -k_3 \times r_2 \quad (5)$$

where the dimensionless proportionality term k_3 can range between 0 and 1. A value of 1 corresponds to ideal stoichiometric mineral dissolution where a pair of $\equiv Mn^{IV}_{edge}$ sites is exposed to allow As(III) adsorption via bidentate-binuclear surface complexation and subsequent oxidation (Zhu et al., 2009). Accordingly, a value of less than 1 for k_3 represents an irregular/unordered arrangement of *newly* exposed $\equiv Mn^{IV}_{edge}$ sites which would impede As(III) adsorption and oxidation.

To consider potential surface passivation from reaction products, surface complexation reactions of As(V) on $\equiv Mn^{IV}_{edge}$ and $\equiv Mn^{III}_{edge}$ sites were included in the reaction network (Tables 1 and 2). At circumneutral pH, adsorption of Mn(II) is favored on negatively charged $\equiv Mn^{IV}_{vacancy}$ sites over $\equiv Mn^{IV}_{edge}$ sites (Simanova et al., 2015). Mn(II) adsorption on positively charged $\equiv Mn^{III}_{edge}$ sites was assumed negligible at circumneutral pH and therefore not considered in the reaction network (Ramstedt et al., 2004). Based on potential surface passivation pathways identified in previous studies (Jiang et al., 2013; Moore et al., 1990; Tournassat et al., 2002), formation of Mn(II)-As(V) precipitates such as a krautite-like mineral ($MnHAsO_4 \cdot H_2O$) and Mn(II)-As(V) ternary complexes on either $\equiv Mn^{IV}_{edge}$ or $\equiv Mn^{IV}_{vacancy}$ sites were also investigated in the modeling framework (Tables 1 and 3).

2.3. Experimental datasets for conceptual model evaluation

Numerous experimental studies, varying in terms of their experimental setups and conditions, have investigated many details of the As(III) oxidation via Mn oxides. Among those, we selected a subset of studies (Lafferty et al., 2011, 2010a; Villalobos et al., 2014) that provided suitable data to elucidate and quantify the role of edge sites and surface passivation on oxidation rates under circumneutral pH conditions. These studies were carried out: (i) with different layered Mn oxide types (δ-MnO_2 and acid birnessite) and SSAs (39, 114 and 273 $m^2\ g^{-1}$); (ii) at different pH values (6.0 and 7.2); (iii) with fixed (batch) and temporally varying inputs (stirred-flow) of either aqueous As(III), As(V) or Mn(II); (iv) as oxidation or adsorption/desorption experiments; and (v) at extended experiment durations (24 and 48 h). The available data showed pronounced temporal variations in the measured aqueous concentrations of As(III), As(V), and Mn(II), and in the calculated concentrations of aqueous and adsorbed total As. The measured aqueous concentrations derived from the adsorption-oxidation experiments using both stirred-flow and batch setups were used for

Table 1
Reaction network and parameter values estimated from the calibration of the stirred-flow oxidation experiment (refer to Table 4 for details) (Lafferty et al., 2010a).

		Parameter values	Relative uncertainty variance reduction #
Surface complexation reactions			
$\equiv \boldsymbol{Mn^{IV}_{edge}}$ Site			
As(III)			
Eq. (6) $2 \equiv Mn^{IV}_{edge}OH + H_3AsO_3 \leftrightarrow (\equiv Mn^{IV}_{edge})_2HAsO_3 + 2H_2O$	log K1	10.75	97.7%
As(V)			
Eq. (7) $2 \equiv Mn^{IV}_{edge}OH + HAsO_4^{2-} \leftrightarrow (\equiv Mn^{IV}_{edge})_2HAsO_4 + 2OH^-$	log K2	−5.69	99.9%
Mn(II)			
Eq. (8) $\equiv Mn^{IV}_{edge}OH + Mn^{2+} + H_2O \leftrightarrow \equiv Mn^{IV}_{edge}OMnOH + 2H^+$	log K3	−6.87	99.7%
$\equiv \boldsymbol{Mn^{III}_{edge}}$ Site			
As(III)			
Eq. (9) $2 \equiv Mn^{III}_{edge}OH + H_3AsO_3 \leftrightarrow (\equiv Mn^{III}_{edge})_2HAsO_3 + 2H_2O$	log K4	8.00	98.7%
As(V)			
Eq. (10) $2 \equiv Mn^{III}_{edge}OH + HAsO_4^{2-} \leftrightarrow (\equiv Mn^{III}_{edge})_2HAsO_4 + 2OH^-$	log K5	insensitive	0
$\equiv \boldsymbol{Mn^{IV}_{vacancy}}$ site			
Mn(II)			
Eq. (11) $\equiv Mn^{IV}_{vacancy}OH + Mn^{2+} + H_2O \leftrightarrow \equiv Mn^{IV}_{vacancy}OMnOH + 2H^+$	log K6	−1.80	14.2%
Mn(II)-As(V) Ternary Surface Complexes			
Eq. (12) $\equiv Mn^{IV}_{edge}OH + MnHAsO_4 \leftrightarrow \equiv Mn^{IV}_{edge}OMnH_2AsO_4$	log K7	insensitive	0
Eq. (13) $\equiv Mn^{IV}_{vacancy}OH + MnHAsO_4 \leftrightarrow \equiv Mn^{IV}_{vacancy}OMnH_2AsO_4$	log K8	insensitive	0
Additional parameters			
Rate constant for oxidation on $\equiv Mn^{IV}_{edge}$ sites (s^{-1}) (Eq. (3))	k_1	1.01×10^{-3}	99.7%
Rate constant for oxidation on $\equiv Mn^{III}_{edge}$ sites (s^{-1}) (Eq. (4))	k_2	1.50×10^{-4}	99.7%
Proportionality term for exposure of new edge surface (dimensionless) (Eq. (5))	k_3	0.67	85.1%
Edge component (mmol L^{-1}) (% of total δ-MnO_2)	C_{edge}	3.70 (32%)	97.0%
Bulk component (mmol L^{-1}) (% of total δ-MnO_2, i.e., 100% - edge component)	C_{bulk}	7.81 (68%)	97.0%
Density of edge sites ($\equiv Mn^{IV}_{edge}$ and $\equiv Mn^{III}_{edge}$) (mol of sites per mol of δ-MnO_2)	s_{edge}	1.13×10^{-1}	99.1%
Density of vacancy sites ($\equiv Mn^{IV}_{vacancy}$) (mol of sites per mol of δ-MnO_2)	$s_{vacancy}$	1.20×10^{-2}	72.4%

Note: #Relative uncertainty variance reduction = 1 - $\frac{\sigma_{ui}^2}{\sigma_i^2}$, where σ_i^2 and σ_{ui}^2 represent prior and posterior variances of parameter i. The "posterior variance" is the estimate of the standard deviation of a parameter after the calibration process has been conducted. Ideally, a reduction is expected between the prior and posterior estimates if the parameter is sensitive. Relative uncertainty variance reduction value of 0 indicates that parameter is insensitive.

Table 2
Additional parameters for batch oxidation experiments (refer to Tables 4 and 5 for details) (Villalobos et al., 2014). All surface complexation constants were consistent with the respectively calibrated values for the stirred-flow experiment (Table 1), although the apparent values were modified based on the SSA and site density of the Mn oxides where appropriate (Sverjensky, 2003). The two reaction rate constants ($\boldsymbol{k}_1$ and $\boldsymbol{k}_2$) were consistent across all batch experiments but differed from those calibrated for the stirred-flow experiment (Table 1).

Experiment ID		B1	B2	B3
Surface Complexation Reactions				
$\equiv \boldsymbol{Mn^{IV}_{edge}}$ Site				
As(III)				
Eq. (6). $2 \equiv Mn^{IV}_{edge}OH + H_3AsO_3 \leftrightarrow (\equiv Mn^{IV}_{edge})_2HAsO_3 + 2H_2O$	log K1	11.59		11.12
As(V)				
Eq. (7). $2 \equiv Mn^{IV}_{edge}OH + HAsO_4^{2-} \leftrightarrow (\equiv Mn^{IV}_{edge})_2HAsO_4 + 2OH^-$	log K2	−4.84		-5.31
Mn(II)				
Eq. (8). $\equiv Mn^{IV}_{edge}OH + Mn^{2+} + H_2O \leftrightarrow \equiv Mn^{IV}_{edge}OMnOH + 2H^+$	log K3	−6.02		-6.49
$\equiv \boldsymbol{Mn^{III}_{edge}}$ Site				
As(III)				
Eq. (9). $2 \equiv Mn^{III}_{edge}OH + H_3AsO_3 \leftrightarrow (\equiv Mn^{III}_{edge})_2HAsO_3 + 2H_2O$	log K4	8.86		8.38
$\equiv \boldsymbol{Mn^{IV}_{vacancy}}$ site				
Mn(II)				
Eq. (11). $\equiv Mn^{IV}_{vacancy}OH + Mn^{2+} + H_2O \leftrightarrow \equiv Mn^{IV}_{vacancy}OMnOH + 2H^+$	log K6	−0.95		-1.42
Additional parameters				
Rate constant for oxidation on $\equiv Mn^{IV}_{edge}$ sites (s^{-1}) (Eq. (3))	k_1	7.94×10^{-3}		
Rate constant for oxidation on $\equiv Mn^{III}_{edge}$ sites (s^{-1}) (Eq. (4))	k_2	6.80×10^{-4}		
Proportionality term for exposure of new edge surface (dimensionless) (Eq. (5))	k_3	0.37	0.20	0.77
Edge component (mmol L^{-1}) (% of total birnessite)	C_{edge}	0.35 (30%)	0.73 (22%)	0.35 (30%)
Bulk component (mmol L^{-1}) (% of total birnessite, i.e., 100% - edge component)	C_{bulk}	0.80	2.59	0.80

Table 3
Reaction network and parameter values sourced from literature and kept fixed during model calibration in this study.

Experiment ID		SF1	B1	B2	B3
Surface protonation/deprotonation reactions					
$\equiv \boldsymbol{Mn^{IV}_{edge}}$ Site	pKa1	4.31 [a]	5.16	5.16	4.69
Eq. (6). $\equiv Mn^{IV}_{edge}OH_2^+ \leftrightarrow \equiv Mn^{IV}_{edge}OH + H^+$	pKa2	6.06 [b]	5.21	5.21	5.68
Eq. (7). $\equiv Mn^{IV}_{edge}OH \leftrightarrow \equiv Mn^{IV}_{edge}O^- + H^+$					
Eq. (8). $\equiv \boldsymbol{Mn^{III}_{edge}}$ Site	pKa	8.20 [c]	9.05	9.05	8.58
$\equiv Mn^{III}_{edge}OH_2^+ \leftrightarrow \equiv Mn^{III}_{edge}OH + H^+$					
Eq. (9). $\equiv \boldsymbol{Mn^{IV}_{vacancy}}$ site	pKa1	1.33 [a]	2.18	2.18	1.71
$\equiv Mn^{IV}_{vacancy}OH_2^+ \leftrightarrow \equiv Mn^{IV}_{vacancy}OH + H^+$	pKa2	2.35 [b]	1.50	1.50	1.97
Eq. (10). $\equiv Mn^{IV}_{vacancy}OH \leftrightarrow \equiv Mn^{IV}_{vacancy}O^- + H^+$					
Additional reactions					
Krautite					
Eq. (11).	log		−0.20 [d]		
$Mn^{2+} + H_2AsO_4^- + H_2O \leftrightarrow MnHAsO_4 \cdot H_2O(s) + H^+$	Ksp				
Mn(II)-As(V) Solution Complexes	log K		1.01 [e]		
Eq. (12). $Mn^{2+} + H_2AsO_4^- \leftrightarrow MnH_2AsO_4^+$	log K		2.92 [e]		
Eq. (13). $Mn^{2+} + HAsO_4^- \leftrightarrow MnHAsO_4(aq)$					

[a] (Peacock and Sherman, 2007).
[b] (Tonkin et al., 2004).
[c] (Ramstedt et al., 2004).
[d] (Tournassat et al., 2002).
[e] (Marini and Accornero, 2007).

Table 4
Experiment details and the derived dataset used for calibration of the numerical model.

Experiment setup	Stirred-flow experiments [a]	Batch experiments [b]		
Dominant reactions	Adsorption + Oxidation	Adsorption + Oxidation		
Experiment ID reference	SF1	B1	B2	B3
Experiment conditions				
Solute and concentration in background electrolyte	0 to 48 h 100 μM As(III)	At 0 h 300 μM As(III)		
Mn oxide				
Type	δ-MnO_2	Acid birnessite		δ-MnO_2
Specific surface area	273 $m^2\ g^{-1}$	39 $m^2\ g^{-1}$		114 $m^2\ g^{-1}$
Amount	11.5 mM	1.15 mM	3.32 mM	1.15 mM
Average Mn oxidation number	3.95	3.93		4.04
pH	7.20	6.00		
Experiment duration	48 h	24 h		
Reaction Cell volume	30 mL	–		
Flow rate	1.0 mL min^{-1}	–		
Data for Model Calibration	Aqueous As(III), As(V) and Mn(II)	Aqueous As(III) and As(V)		

[a] (Lafferty et al., 2010a).
[b] (Villalobos et al., 2014).

calibration of the numerical model (Table 4) whereas the remainder of the dataset was used for verification of the calibrated model (Table 5).

2.4. Numerical modeling tools and calibration

A total of four stirred-flow and five batch experiments were simulated in this study using a common set of model parameters. Among the employed model parameters, we distinguished between the ones that must be fundamentally similar for all experiments and those that may differ between experiments depending on experimental setups and conditions. The former included surface complexation constants and site densities. The equilibrium constants were derived from the calibration of the stirred-flow model, and where appropriate modified based on their SSA and site density according to the approach described by Sverjensky (2003) and further elaborated for SCMs that include bidentate adsorption by Wang and Giammar (2013). The two reaction rate constants (k_1 and k_2) were consistent across all batch experiments but differed from those calibrated for the stirred-flow experiments. This difference was introduced to account for potential differences in the solution saturation state that could arise between the two types of reactors, due to the accumulation of reaction products within batch systems, which can affect dissolution kinetics (Kraemer and Hering, 1997). The other two calibrated parameters, the proportionality term (k_3) and the edge concentration (C_{edge}), varied across the experiments as mineral properties of different Mn oxides varied between the studies.

All batch simulations were performed with PHREEQC (Parkhurst and Appelo, 2013) while the stirred-flow experi-

Table 5
Experiment details and the derived dataset used for verification of the numerical model.

Experiment setup	Stirred-flow experiments[a,b]				Batch experiments[c]	
Dominant reactions	Adsorption + Oxidation	Adsorption + Oxidation + Desorption	Adsorption		Adsorption	
Experiment ID reference	SF1	SF2	SF3	SF4	B4	B5
Experiment conditions						
Solute and concentration in background electrolyte	0 to 48 h 100 µM As(III)	0 to 24 h – 100 µM As(III) 24 to 48 h – 0 µM As(III)	0 to 48 h 100 µM As(V)	0 to 48 h 100 µM Mn(II)	At 0 h varying As(V)	
Mn oxide						
Type	δ-MnO_2				Acid birnessite	δ-MnO_2
Specific surface area	273 m^2 g^{-1}				39 m^2 g^{-1}	144m^2 g^{-1}
Amount	11.5 mM				4.02 mM	
pH	7.20				6.00	
Experiment duration	48 h				24 h	
Reaction Cell volume	30 mL				–	
Flow rate	1.0 mL min^{-1}				–	
Data for Model Verification						
	Total As adsorbed	Aqueous As(III) and As(V)	Aqueous As(V)	Aqueous Mn(II)	Aqueous As(V)	

[a] (Lafferty et al., 2010a).
[b] (Lafferty et al., 2011).
[c] (Villalobos et al., 2014).

ments were simulated with MODFLOW (Harbaugh, 2005) and PHT3D (Prommer et al., 2003) to account for flow and reactive processes, respectively. The standard WATEQ4F database (Ball and Nordstrom, 1991) was used as a starting point for the reaction network definition to which our newly defined reactions were added. For example, the edge ($\equiv Mn^{IV}_{edge}$) and vacancy ($\equiv Mn^{IV}_{vacancy}$) sites were defined in the database and their protonation-deprotonation constants (pKa) were adopted from the literature for birnessite (Peacock and Sherman, 2007; Tonkin et al., 2004) whereas, the values for $\equiv Mn^{III}_{edge}$ sites were adopted from the constants provided for manganite (Ramstedt et al., 2004) and not varied any further (Table 3). Edge and vacancy site densities reported in a birnessite study (Villalobos, 2015) were used as starting values and subsequently varied during model calibration (Table 1). As(III) and As(V) were decoupled from the global redox equilibrium and their redox transformations were kinetically controlled. The SCM was restricted to considering only the chemical contribution towards the overall adsorption, and the electrostatic effects on the complexation were ignored. This was because the SSA of end-basal planes and edge surface of a Mn oxide particle cannot be determined separately (Villalobos et al., 2014), which is required for the calculation of surface charge on vacancy and edge sites in a SCM. Similar to many published modeling studies (Rathi et al., 2017b,a; Stolze et al., 2019; Sun et al., 2018), given that reactants were sufficiently mixed/stirred in the investigated experimental systems all surface complexation reactions were assumed to be sufficiently fast such that the local-equilibrium assumption (Bahr and Rubin, 1987) was valid. Initial estimates of the reaction constants for As(III), As(V) and Mn(II) surface complexation on respective sites were estimated via manual calibration and further optimized during an automated calibration step. The solubility product of the Mn(II)-As(V) precipitate krautite and the constants for Mn(II)-As(V) solution complexes were set to literature values (Tournassat et al., 2002) and not varied any further (Table 3).

Each model calibration run included multiple model simulations, where each simulation corresponded to one of the oxidation experiments (Table 4). We employed initially a manual trial-and-error step, followed by an automatic calibration step using the heuristic particle swarm optimization (PSO) (Coello et al., 2004; Eberhart and Kennedy, 1995; Kennedy et al., 2001) algorithm. PSO was chosen because it has previously been shown to be a suitable method for dealing with the non-linearity of complex geochemical models (Jamieson et al., 2018; Prommer et al., 2018; Rathi et al., 2017a,b; Sun et al., 2018). The PSO code was written within the PEST++ platform using the PANTHER run manager and linked with PHREEQC/PHT3D (Siade et al., 2019). The 12 parameters to be estimated included surface complexation constants for As(III), As(V), Mn(II) and Mn(II)-As(V) ternary complexes, oxidation rate constants (k_1 and k_2), proportionality term (k_3), surface site densities (s_{edge} and $s_{vacancy}$), and C_{edge} (Tables 1 and 2). Calibration was achieved by minimizing the objective function defined as the sum of squared residuals between all observations from the considered experiments (Table 4) and their model-simulated equivalents. The calibrated model was further verified against the observations from various stirred-flow and batch experiments (Table 5) (Lafferty et al., 2011, 2010a; Villalobos et al., 2014). Finally, the parameter estimates from PSO calibration were used as initial values for a linearized parameter uncertainty analysis using PEST (Doherty, 2015; Rathi et al., 2017b; Rawson et al., 2017); further details are provided in Table 1.

3. Results

3.1. Quantification of As(III) oxidation rates

The final calibrated models closely replicated the observations from As(III) oxidation experiments conducted using both stirred-flow (Table 4 and Fig. 2a) and batch setups (Table 4 and Fig. 3a). Moreover, they also reproduced all observations available from the oxidation and adsorption experiments (Table 5) for the purpose of model verification (Figs. 2a and 4). The model-based analysis demonstrated that the As(III) oxidation rates show two distinct phases in the batch experiments but three distinct phases in the stirred-flow experiments.

Phase I was identified in all of the analyzed experiments and characterized by fast As(III) oxidation. During Phase I, high solution As(III) saturated the sorption sites and was completely oxidized and released into the solution as As(V). The length of Phase I ranged between only a few minutes to a few hours (Figs. 2a and 3a). The amount of C_{edge} regulated the duration of Phase I and the

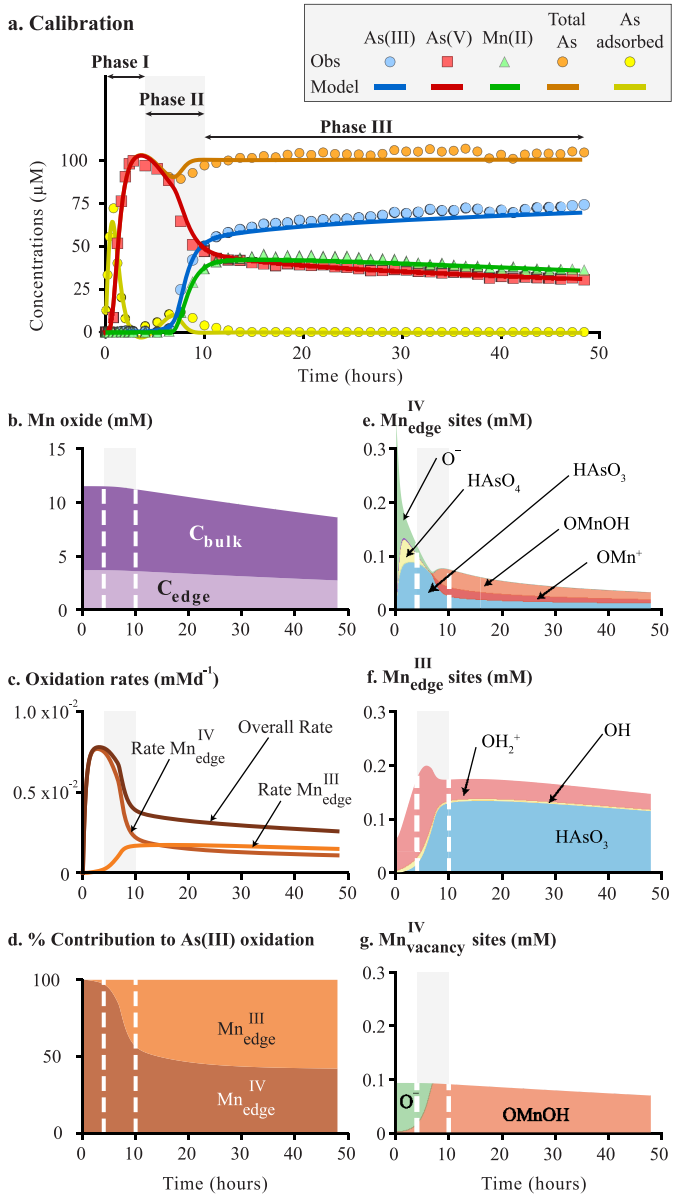

Fig. 2. Simulations and observations (where available) from stirred-flow oxidation experiment (Lafferty et al., 2010a). Panel a: calibrated model output against observations and three phases of As(III) oxidation by Mn oxide. Panel b: changes in the Mn oxide concentrations ($\mathbf{C_{edge}}$ and $\mathbf{C_{bulk}}$) during the experiment. Panel c: oxidation rates – overall and on each type of edge site ($\equiv \mathbf{Mn^{IV}_{edge}}$ and $\equiv \mathbf{Mn^{III}_{edge}}$). Panel d: percentage contribution to As(III) oxidation by each type of edge site. Panels e, f and g show adsorbed species on edge and vacancy sites.

experimental data within this phase were critical for the estimation of C_{edge}. The variations in the model-estimated values for C_{edge} among the different experiments reflect the differences in the initial concentrations and types of Mn oxides used (Figs. 2b and 3). When the same initial concentration but different Mn oxides were used (Table 2), C_{edge} was higher for δ-MnO_2 compared to acid birnessite due to the higher edge surface area (Villalobos et al., 2014) of δ-MnO_2. On the other hand, when different amounts of the same Mn oxide were used (e.g., Table 2, B1 vs B2), higher C_{edge} values reflected higher initial concentrations of the mineral added in the experiments. However, for a given type of Mn oxide, the proportion of C_{edge} on the mineral was comparable irrespective of the experimental setup (Tables 1 and 2). In the stirred-flow oxidation experiment, as determined by oxalate titration (Villalobos et al., 2003), the AMON of δ-MnO_2 was 3.95 (Lafferty et al., 2010a). Therefore, C_{edge} in the numerical model was assigned to host 95% of $\equiv Mn^{IV}_{edge}$ and 5% of $\equiv Mn^{III}_{edge}$ sites at the start of the experiment. During Phase I, $\equiv Mn^{IV}_{edge}$ sites were reduced to $\equiv Mn^{III}_{edge}$ sites and no Mn(II) was produced (Fig. 2a). In conjunction with the reductive transformation, the AMON decreased to 3.80 (Fig. S1). Common to all experiments the end of Phase I was marked by a distinct decrease in the overall oxidation rate (Figs. 2c and S1b).

In the stirred-flow experiment, Phase I was followed by a transition phase (Phase II) where As(III) oxidation gradually shifted from fast reacting $\equiv Mn^{IV}_{edge}$ to slow reacting $\equiv Mn^{III}_{edge}$ sites. This caused the overall oxidation rate to decrease significantly (Figs. 2c). During this transition small amounts of As(III) remained adsorbed on $\equiv Mn^{III}_{edge}$ sites (Fig. 2f) due to the significantly slower oxidation rates. This can explain the observed temporary decrease in total dissolved As concentrations (Fig. 2a). Phase II lasted for a relatively short period (from $t = 4$ h to 10 h) in the stirred-flow experiment. The duration of Phase II depended upon the availability of both, the initially present $\equiv Mn^{IV}_{edge}$ sites and the newly formed $\equiv Mn^{III}_{edge}$ sites on C_{edge} (Fig. 2e and f). During Phase II, the $\equiv Mn^{III}_{edge}$ sites were slowly reduced to Mn(II), causing mineral dissolution on the edge surface while a *new* edge surface on C_{bulk} was exposed, which hosted *new* $\equiv Mn^{IV}_{edge}$ sites. However, the amount of newly exposed edge sites was only 67% of the "parent" edge sites ($k_3 = 0.67$, with relative uncertainty variance reduction of 85.1%, Table 1), i.e., a net decrease of C_{edge} occurred. Slower oxidation of As(III) produced lower amounts of As(V) in solution while Mn(II) was gradually produced and a fraction of it was adsorbed first on $\equiv Mn^{IV}_{vacancy}$ sites and then on $\equiv Mn^{IV}_{edge}$ sites (Fig. 2e and g). The AMON of δ-MnO_2 dropped to 3.72 during Phase II since the slow reactivity of the $\equiv Mn^{III}_{edge}$ sites promoted an accumulation of Mn(III) on the mineral edge surface (Fig. S1). Finally, Phase III in the stirred-flow experiment was identifiable by a relatively constant oxidation rate that occurred when the continuous As(III)-bearing influent to the reactor started to reach a steady-state with the overall As(III) oxidation on both $\equiv Mn^{III}_{edge}$ and *new* $\equiv Mn^{IV}_{edge}$ sites. Hence, effluent As(III), As(V) and Mn(II) concentrations remained constant during Phase III. Dissolution of δ-MnO_2 continued on the edge surface as indicated by the steady decrease in C_{edge} value. Corresponding to the achieved steady state, AMON of δ-MnO_2 did not change any further during Phase III (Fig. S1).

In contrast, no transition Phase II was identified during any of the As(III) oxidation batch experiments. Instead, there was a direct transition from Phase I to a steady rate phase that resembled Phase III of the stirred-flow experiment (Fig. 3). Based on the model simulations, the absence of Phase II can be attributed either to low initial As(III) concentrations (Table 4, B2) or, as in B1 and B3, to the low initial amount of Mn oxide. During Phase I, all $\equiv Mn^{IV}_{edge}$ sites on C_{edge} collectively oxidized As(III) and were themselves reduced to $\equiv Mn^{III}_{edge}$ sites. Subsequently in Phase III, oxidation was dominated on $\equiv Mn^{III}_{edge}$ sites with only minor contributions from the *new* $\equiv Mn^{IV}_{edge}$ sites.

4. Discussion

4.1. Factors controlling the rate of As(III) oxidation

4.1.1. Type and abundance of edge sites

The type of edge sites, $\equiv Mn^{IV}_{edge}$ or $\equiv Mn^{III}_{edge}$, and their abundances on Mn oxides were found to be the two most important factors that determine As(III) oxidation rate. This is best seen in the simulation of the stirred-flow experiment where the abundance of fast reacting $\equiv Mn^{IV}_{edge}$ sites decreased considerably after Phase

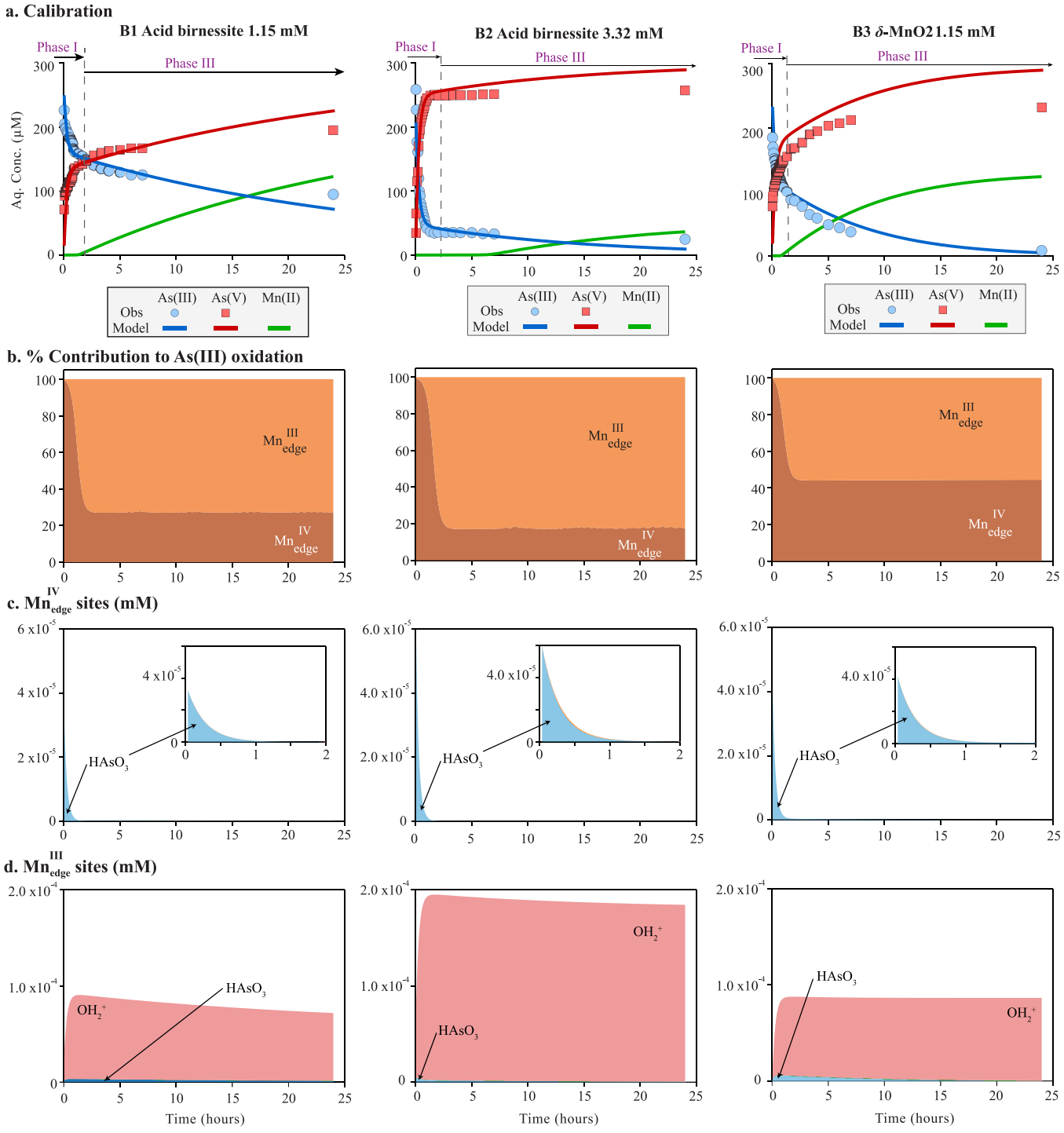

Fig. 3. Simulations and observations (where available) from batch oxidation experiments (Villalobos et al., 2014). Row a: calibrated model results against observations from three batch experiments. Row b: percentage contribution to As(III) oxidation by each type of edge site ($\equiv \mathbf{Mn^{IV}_{edge}}$ and $\equiv \mathbf{Mn^{III}_{edge}}$). Rows c and d show adsorbed species on $\equiv \mathbf{Mn^{IV}_{edge}}$ and $\equiv \mathbf{Mn^{III}_{edge}}$ sites, respectively.

I while that of slow reacting $\equiv Mn^{III}_{edge}$ sites started to increase during Phase II. During Phase III, $\equiv Mn^{III}_{edge}$ sites were more abundant than $\equiv Mn^{IV}_{edge}$ sites but both edge sites gradually depleted at a steady rate (Fig. 2e and f). Accordingly, As(III) oxidation rates were highest when a large number of $\equiv Mn^{IV}_{edge}$ sites was available (Phase I), modest for a combination of both $\equiv Mn^{IV}_{edge}$ and $\equiv Mn^{III}_{edge}$ sites (Phase II) and lowest when $\equiv Mn^{III}_{edge}$ sites were predominant (Phase III) (Fig. 2c). In contrast, the simulations of the batch experiments showed that As(III) oxidation over most of the experimental duration was controlled by the abundance of only $\equiv Mn^{III}_{edge}$ sites while the influence of $\equiv Mn^{IV}_{edge}$ sites was only visible during the short Phase I. The simulations of the batch experiments showed that either most of the added As(III) was oxidized within Phase I by an excess amount of initially available $\equiv Mn^{IV}_{edge}$ sites or, conversely, excess As(III) completely reduced $\equiv Mn^{IV}_{edge}$ to $\equiv Mn^{III}_{edge}$ sites during Phase I before oxidation continued on the remaining $\equiv Mn^{III}_{edge}$ sites (Fig. 3).

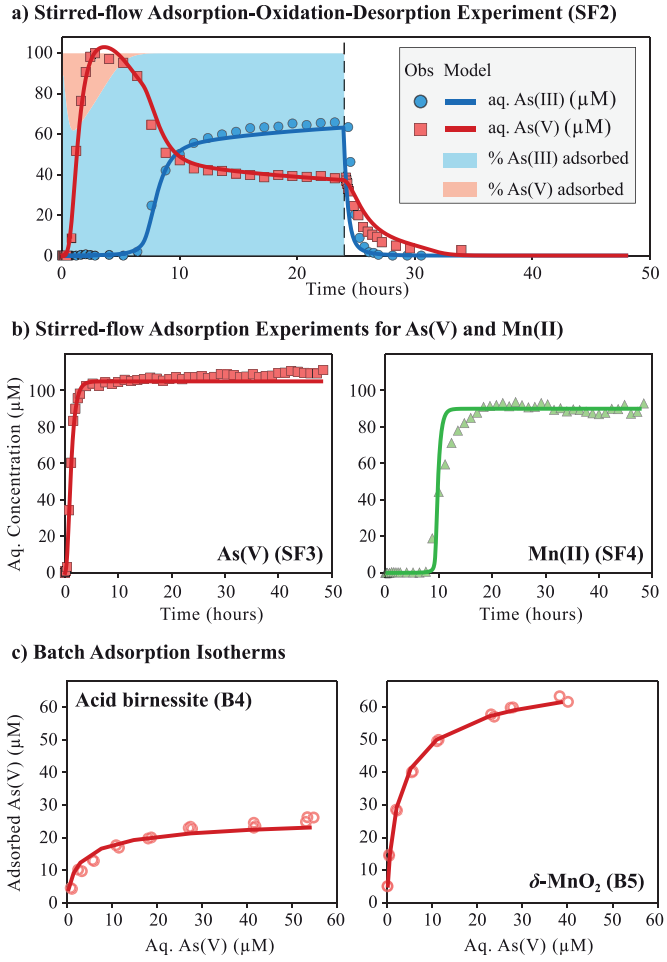

Fig. 4. Observations and model simulation of the stirred-flow (Table 5, SF2-SF4) and batch experiments (Table 5, B4-B5) (Lafferty et al., 2011, 2010a; Villalobos et al., 2014). The datasets were used for verification of the calibrated numerical model.

During Phases II and III of the stirred-flow oxidation experiment, our model simulation showed a disparity in the rates of exposing new C_{edge} versus dissolution of the parent C_{edge}, as indicated by an estimated value of 0.67 for k_3 (Table 1). This could be interpreted as having only two out of every three newly exposed $\equiv Mn^{IV}_{edge}$ sites present adjacent to each other to allow for As(III) adsorption to occur via a bidentate-binuclear surface complex. This reduced efficiency could be a result of the difference in the As(III) oxidation rates between $\equiv Mn^{IV}_{edge}$ and $\equiv Mn^{III}_{edge}$ sites, which causes accumulation of $\equiv Mn^{III}_{edge}$ sites compared to $\equiv Mn^{IV}_{edge}$. As a result, a *new* $\equiv Mn^{IV}_{edge}$ site can become isolated on the *new* edge surface, jeopardizing their As(III) oxidation ability. (Fig. 1). The value of k_3 also appears to be a function of the mineral SSA. In the batch experiments, k_3 ranged between 0.20 and 0.27 for acid birnessite with an SSA of 39 $m^2\ g^{-1}$ while it was 0.78 for δ-MnO_2 with an SSA of 114 $m^2\ g^{-1}$ (Table 2).

Furthermore, the lower oxidation rate on Mn^{III}_{edge} sites might have led to a longer retention time of adsorbed As(III) on these sites before undergoing oxidation. This hypothesis was supported by the temporary decrease in the total dissolved As concentrations that is apparent during Phase II of the stirred-flow oxidation experiment (Fig. 2). To test this hypothesis, we used the calibrated model to simulate a stirred-flow adsorption-oxidation-desorption experiment (Table 5, SF2) (Lafferty et al., 2011). In this experiment, the As(III)-bearing influent was switched over to an As(III)-free background electrolyte after 24 h to initiate a desorption phase. The dilution curve suggested a lag time of ~3 h for the influent to fully saturate the reactor. Arsenic speciation analysis on the collected samples showed that As associated with δ-MnO_2 was present as As(V) and no As(III) was observed in the effluent during the desorption phase (Lafferty et al., 2011). However, our model simulation suggested that As associated with δ-MnO_2 would temporarily remain as As(III). The adsorbed As(III) was then oxidized to As(V) over the lag time of dilution during the desorption phase (Fig. 4a) and before the *ex-situ* solid-phase As speciation analysis with EXAFS was performed.

4.1.2. Surface passivation

The model simulations of the stirred-flow experiment showed that passivation of $\equiv Mn^{IV}_{edge}$ sites by As(V) was minor and occurred only during Phase I (Fig. 2e). During Phase II, Mn(II) saturated the $\equiv Mn^{IV}_{vacancy}$ sites, which contributed to its delayed release into the solution. Subsequently, Mn(II) competed with both As(III) and As(V) for adsorption on $\equiv Mn^{IV}_{edge}$ sites (Fig. 2e and g). Since $\equiv Mn^{IV}_{edge}$ sites are mostly negatively charged ($\equiv Mn^{IV}_{edge}O^-$) at pH 7.20 (Peacock and Sherman, 2007; Tonkin et al., 2004), adsorption of Mn(II) is favored over neutral As(III) (H_3AsO_3) and negatively charged As(V) ($HAsO_4^{2-}$) species. After 9 h into the experiment, coverage by total adsorbed Mn(II) with respect to the total amount of sorption sites (36%) exceeded that of As(III) and As(V) combined (30%). Surface passivation by Mn(II) was exclusively responsible for restricting As(III) oxidation on *new* $\equiv Mn^{IV}_{edge}$ sites, limiting further production of $\equiv Mn^{III}_{edge}$ sites, and, thereby, regulating the overall duration of Phase II. Interestingly, based on the model simulations, passivation of positively charged $\equiv Mn^{III}_{edge}$ sites by As(V) oxyanions was minor (Fig. 2f). This was in contrast to the expected higher affinity of negatively charged As(V) compared to the neutral As(III) species at pH 7.20 (Ramstedt et al., 2004; Zhu et al., 2009). The continuous influx of high As(III) concentrations into the reactor might have prevented competitive adsorption of As(V) during Phases II and III.

In contrast to the stirred-flow experiments, surface passivation by either As(V) or Mn(II) was not apparent in the batch experiments. This is because early in these experiments, As(III) oxidation transitioned directly into Phase III. During Phase III, Mn oxides predominantly hosted $\equiv Mn^{III}_{edge}$ sites which were saturated by As(III) (Fig. 3c and d).

Potential surface passivation by krautite and Mn(II)-As(V) ternary surface complexes was also evaluated. Using the literature value for the solubility product of krautite (Tournassat et al., 2002), our simulations showed that krautite never reached saturation in any of the experiments analyzed. Therefore, surface passivation by krautite most likely only occurs at extremely high concentrations of Mn(II) and As(V), which are rarely seen in environmental settings. As there are no surface complexation constants available for the Mn(II)-As(V) ternary surface complexes, they were treated as adjustable during model calibration but found to be insensitive with respect to the employed observation data (Table 1). Therefore, surface passivation by Mn(II)-As(V) ternary surface complexes could not be quantified in this study.

4.2. Parameter sensitivity analysis

4.2.1. Manual sensitivity analysis for selected parameters

Additional model runs were conducted with one of the parameters being adjusted by a small amount (±20%) from its calibrated value while keeping the remaining parameters consistent with the calibrated model. The results of the model simulations for four key parameters show that they affect As(III) oxidation during different

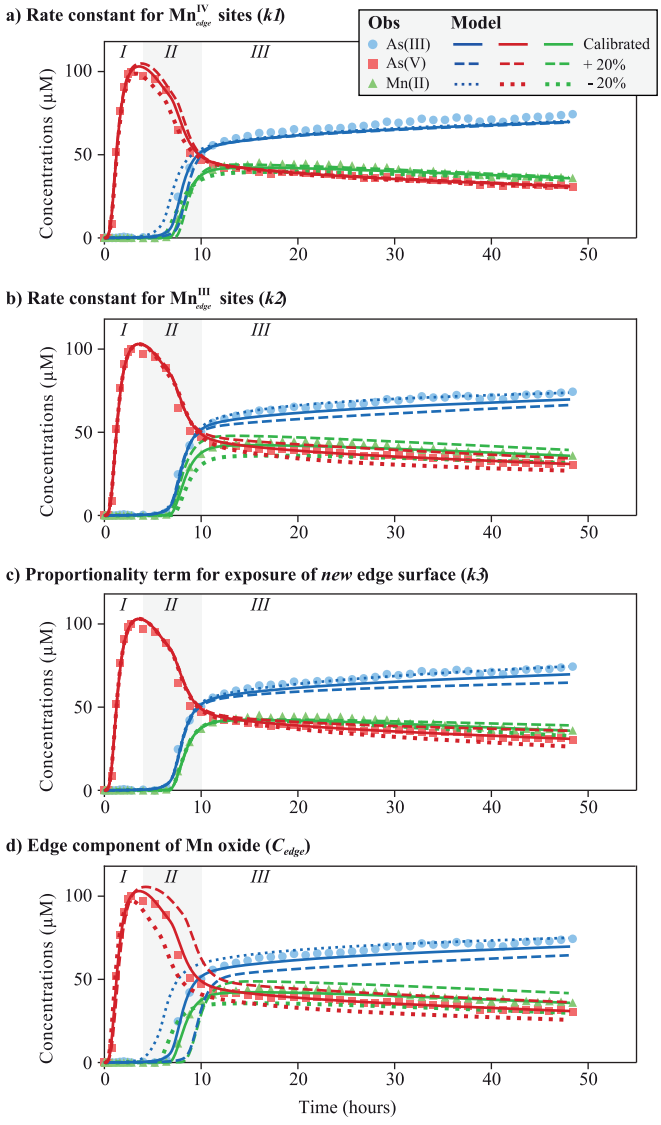

Fig. 5. Sensitivity of key parameters demonstrated quantitatively through model predictions by adjusting only the corresponding parameter values by ±20% while keeping the remaining parameters consistent with their calibrated values.

phases (Fig. 5). For example, the effect of rate constant k_1 was visible only during oxidation Phase II when the amount of adsorbed As on $\equiv Mn^{IV}_{edge}$ sites is comparable to k_1 (Eq. (3) and Fig. 2e). Similarly, the effects of the rate constant k_2 were visible only during Phase III. Interestingly, the influence of the proportionality term k_3 is visible only during the tail-end of Phase III after the rate of oxidation on $\equiv Mn^{III}_{edge}$ sites surpasses that on $\equiv Mn^{IV}_{edge}$ sites (Fig. 2c). This suggests that k_3 has a direct effect on the long-term oxidation rate of As(III). Finally, the influence of the edge component (C_{edge}) on oxidation is visible only after As(III) is predominantly adsorbed on $\equiv Mn^{III}_{edge}$ sites, i.e., during Phase II and III (Fig. 2e and f).

4.2.2. Parameter uncertainty variance reduction

Beside the manual sensitivity analysis, an automatic linearized uncertainty analysis, based on local parameter sensitivities, was also conducted for the simulation of the stirred-flow experiments. Although due to the highly nonlinear nature of the simulated processes, the results of this linearized statistical analysis should be interpreted with caution, the analysis was able to recognize the parameters that were well-constrained by the selected datasets and those that were less constrained or insensitive during model calibration (Table 1). The insensitive parameters included surface complexation constant of As(V) on $\equiv Mn^{III}_{edge}$ (log K5), and ternary surface complexes on $\equiv Mn^{IV}_{edge}$ (log K9) and $\equiv Mn^{IV}_{vacancy}$ (log K10) sites. Although these insensitive parameters did not influence the model outcomes under the tested experimental conditions, the possibility of these processes playing a role under other conditions cannot be ruled out. In addition, the parameter describing surface complexation of Mn(II) on $\equiv Mn^{IV}_{vacancy}$ sites (log K6) was sensitive, but its low reduction in relative uncertainty (i.e., 14.2%) suggests that the reported parameter value was not uniquely identifiable (Table 1). This implies that this parameter can potentially take on a range of values while still achieving a good model calibration; however, this parameter's sensitivity is relatively low compared to the other parameters, indicating that its low reduction in posterior variance is not likely due to the correlation that results from over-parameterization. These results demonstrate that inverse problem for this study was relatively well-determined.

Furthermore, sensitivity analysis of the stirred-flow model indicated a strong negative correlation between several parameters that represent competing processes. For example, negative correlation between the surface complexation constants for As(III) (log K1) and Mn(II) (log K3) on $\equiv Mn^{IV}_{edge}$ sites (Table S1) is understandable because both species compete for sorption on these sites.

5. Conclusions

Using a process-based modeling approach, this study evaluated a conceptual model that reflects the widely accepted mechanisms for As(III) oxidation by Mn oxides. Based on the modeling results, the rate of As(III) oxidation by Mn oxides is controlled by the accessibility to both $\equiv Mn^{IV}_{edge}$ and $\equiv Mn^{III}_{edge}$ sites and by surface passivation from Mn(II). A transitional Phase II, which was clearly identified in the stirred flow experiment but not in the batch system, represents a period when As(III) oxidation gradually shifts from fast reacting $\equiv Mn^{IV}_{edge}$ to slowly reacting $\equiv Mn^{III}_{edge}$ sites. Under conditions typical of natural groundwater systems with flow, oxidation of aqueous As(III) by Mn oxides may also follow a three phase reaction mechanism.

Our modeling results suggest that several previous studies that used a batch reactor setup possibly overestimated the importance of $\equiv Mn^{IV}_{edge}$ sites for As(III) oxidation. These sites were only responsible for As(III) oxidation during a brief initial phase. Subsequently, oxidation occurs predominantly on $\equiv Mn^{III}_{edge}$ sites at slow rates, allowing for retention of adsorbed As(III). In contrast, a stirred-flow reactor setup in which reactant concentrations are additionally affected by flow rates is generally more relevant for studying natural groundwater systems or a water treatment plant, and allows for a more detailed inspection of the complex reaction network. Based on the dataset from the stirred-flow experiment, a three-phase As(III) oxidation mechanism has been identified, which is driven by the accessibility to both $\equiv Mn^{IV}_{edge}$ and $\equiv Mn^{III}_{edge}$ sites and regulated by solution pH and surface passivation from Mn(II). The abundance of $\equiv Mn^{IV}_{edge}$ sites corresponds to rapid oxidation while that of $\equiv Mn^{III}_{edge}$ sites would correspond to adsorption and steady but slower oxidation.

Despite the good agreement of our model simulations with the tested literature datasets, a universal applicability of the derived parameters, such as oxidation rate constants, is not prudent because several model parameters were insensitive and one model parameter was not well constrained in this study. To reduce uncertainty in the model conceptualization and parameter values, and to improve robustness and wider applicability, continued research effort from both experimentalists and modelers is clearly required. Nonetheless, the numerical model presented here derived several

hypotheses which can assist in the design of future experiments. For example, model simulations of experiments with δ-MnO_2 and acid birnessite showed that varying particle sizes regulated the value of C_{edge} which in turn means a higher abundance of edge sites. This finding could be extended to and verified on other layered and even tunnel structured Mn oxides. Similarly, model simulations show that all adsorbed As persisted as As(III) for longer on slow reacting $\equiv Mn^{III}_{edge}$ sites. However, the delays in sample collection and measurements might have allowed oxidation of adsorbed As(III) to As(V) before samples were analyzed. This hypothesis could be tested with *in-situ* measurements of adsorbed As such as the quick-scanning XAS technique (Ginder-Vogel et al., 2009). Furthermore, the current model framework can be extended to study the reactivity of other Mn oxides, e.g., tunnel structured or Mn oxides with impurity (Power et al., 2005), effects of competing solutes, e.g., Fe(II) (Wu et al., 2015), other redox-sensitive pollutants, e.g., Cr (Eary and Rai, 1987) and micro organic pollutants (Furgal et al., 2014), as well as effects of a wider range of solution pH (Wu et al., 2015) and comproportionation (Lafferty et al., 2010b; Wang et al., 2019, 2018; Zhao et al., 2016). The extended model(s) can be subsequently used to design new experiments where the experimental conditions can be optimized and the most informative data sampling campaign can be determined ahead of time.

Growing application of Mn oxides in wastewater treatment (Husnain et al., 2020) demands that future work should be expanded towards analysis of experiments where raw influent is treated with Mn oxides. However, due to a more complex matrix, numerous constituents in the raw water would compete for reactions with Mn oxides and therefore, a detailed knowledge of each reaction mechanism will be required for the development of a numerical model. Our present study represents an important milestone towards this goal and the numerical model developed here could assist with the design of new experiments for the purpose of gaining the required insight into the mechanism of Mn oxide reaction with various raw water constituents.

Declaration of Competing Interest

The authors declare that they have no known competing financial interests or personal relationships that could have appeared to influence the work reported in this paper.

Acknowledgments

J.S. is grateful to support from the Strategic Priority Research Program of Chinese Academy of Sciences (Grant # XDB40000000). B.R. would like to acknowledge the funding provided by Deutsche Forschungsgemeinschaft (DFG) through AdvectAs project (DACH grant # 200021E-167821), the University of Western Australia (UWA) for a University Postgraduate Award, and the computing facilities and other infrastructure provided by CSIRO Land and Water. M.Z. is grateful to support of United States National Science Foundation (EAR-1529937). The authors would also like to thank B. Lafferty, M. Villalobos, C. Salazar-Camacho and I. Escobar-Quiroz for providing experimental data in raw format, which was essential for the completion of this study. We thank D.K. Nordstrom and Kamlesh Rathi for their valuable input.

Supplementary materials

Supplementary material associated with this article can be found, in the online version, at doi:10.1016/j.watres.2020.116195.

References

Amirbahman, A., Kent, D.B., Curtis, G.P., Davis, J.A., 2006. Kinetics of sorption and abiotic oxidation of arsenic(III) by aquifer materials. Geochim. Cosmochim. Acta 70, 533–547. doi:10.1016/j.gca.2005.10.036.

Bahr, J.M., Rubin, J., 1987. Direct comparison of kinetic and local equilibrium formulations for solute transport affected by surface reactions. Water Resour. Res. 23, 438–452. doi:10.1029/WR023i003p00438.

Bai, Y., Yang, T., Liang, J., Qu, J., 2016. The role of biogenic Fe-Mn oxides formed in situ for arsenic oxidation and adsorption in aquatic ecosystems. Water Res. 98, 119–127. doi:10.1016/j.watres.2016.03.068.

Ball, J.W., Nordstrom, D.K., 1991. User's manual for WATEQ4F, with revised thermodynamic data base and text cases for calculating speciation of major, trace, and redox elements in natural waters Open-File Report.

Coello, C.A.C., Pulido, G.T., Lechuga, M.S., 2004. Handling multiple objectives with particle swarm optimization. Evol. Comput. IEEE Trans. 8, 256–279. doi:10.1109/TEVC.2004.826067.

Davis, J.A., Kent, D.B., 1990. Surface complexation modeling in aqueous geochemistry. In: Hochella, M.F., White, A.F. (Eds.), Mineral-Water Interface Geochemistry. Miner. Soc. Am., Washington, pp. 177–260.

De Rudder, J., Van De Wiele, T., Dhooge, W., Comhaire, F., Verstraete, W., 2004. Advanced water treatment with manganese oxide for the removal of 17α-ethynylestradiol (EE2). Water Res. 38, 184–192. doi:10.1016/j.watres.2003.09.018.

Doherty, J., 2015. Calibration and Uncertainty Analysis for Complex Environmental Models Brisbane.

Driehaus, W., Seith, R., Jekel, M., 1995. Oxidation of arsenate(III) with manganese oxides in water treatment. Water Res. 29, 297–305. doi:10.1016/0043-1354(94)E0089-O.

Du, J., Xiao, G., Xi, Y., Zhu, X., Su, F., Kim, S.H., 2020. Periodate activation with manganese oxides for sulfanilamide degradation. Water Res. 169. doi:10.1016/j.watres.2019.115278, 115278.

Eary, L.E., Rai, D., 1987. Kinetics of chromium(III) oxidation to chromium(VI) by reaction with manganese dioxide. Environ. Sci. Technol. 21, 1187–1193. doi:10.1021/es00165a005.

Eberhart, R., Kennedy, J., 1995. A new optimizer using particle swarm theory. In: Proceedings of the Sixth International Symposium on Micro Machine and Human Science, 1995, 95. MHS, pp. 39–43. doi:10.1109/MHS.1995.494215.

Fendorf, S., Michael, H.A., van Geen, A., 2010. Spatial and temporal variations of groundwater arsenic in South and Southeast Asia. Science 328 (80), 1123–1127. doi:10.1126/science.1172974.

Feng, X., Wang, P., Shi, Z., Kwon, K.D., Zhao, H., Yin, H., Lin, Z., Zhu, M., Liang, X., Liu, F., Sparks, D.L., 2018. A quantitative model for the coupled kinetics of arsenic adsorption/desorption and oxidation on manganese oxides. Environ. Sci. Technol. Lett. 5, 175–180. doi:10.1021/acs.estlett.8b00058.

Furgal, K.M., Meyer, R.L., Bester, K., 2014. Removing selected steroid hormones, biocides and pharmaceuticals from water by means of biogenic manganese oxide nanoparticles in situ at ppb levels. Chemosphere 136, 321–326. doi:10.1016/j.chemosphere.2014.11.059.

Ginder-Vogel, M., Landrot, G., Fischel, J.S., Sparks, D.L., 2009. Quantification of rapid environmental redox processes with quick-scanning x-ray absorption spectroscopy (Q-XAS). Proc. Natl. Acad. Sci. 106, 16124–16128. doi:10.1073/pnas.0908186106.

Gude, J.C.J., Rietveld, L.C., van Halem, D., 2017. As(III) oxidation by MnO_2 during groundwater treatment. Water Res. 111, 41–51. doi:10.1016/j.watres.2016.12.041.

Harbaugh, A.W., 2005. MODFLOW-2005: the U.S. Geological Survey modular ground-water model - the ground-water flow process. B. 6 model. Tech. Sect. A. Ground-water.

Hu, E., Pan, S., Zhang, W., Zhao, X., Liao, B., He, F., 2019. Impact of dissolved O_2 on phenol oxidation by δ-MnO_2. Environ. Sci. Process. Impacts 21, 2118–2127. doi:10.1039/c9em00389d.

Huling, J.R., Huling, S.G., Ludwig, R., 2017. Enhanced adsorption of arsenic through the oxidative treatment of reduced aquifer solids. Water Res. 123, 183–191. doi:10.1016/j.watres.2017.06.064.

Husnain, S.M., Asim, U., Yaqub, A., Shahzad, F., Abbas, N., 2020. Recent trends of MnO_2-derived adsorbents for water treatment: a review. New J. Chem. doi:10.1039/c9nj06392g.

Jamieson, J., Prommer, H., Kaksonen, A.H., Sun, J., Siade, A.J., Yusov, A., Bostick, B., 2018. Identifying and quantifying the intermediate processes during nitrate-dependent iron(II) oxidation. Environ. Sci. Technol. 52, 5771–5781. doi:10.1021/acs.est.8b01122.

Jenne, E.A., 1968. Controls on Mn, Fe, Co, Ni, Cu, and Zn concentrations in soils and water: the significant role of hydrous Mn and Fe oxides. In: Trace Inorganics In Water. American Chemical Society, pp. 337–387. doi:10.1021/ba-1968-0073.ch02110.1021/ba-1968-0073.ch021.

Jiang, W., Lv, J., Luo, L., Yang, K., Lin, Y., Hu, F., Zhang, J., Zhang, S., 2013. Arsenate and cadmium co-adsorption and co-precipitation on goethite. J. Hazard. Mater. 262, 55–63. doi:10.1016/J.JHAZMAT.2013.08.030.

Kennedy, J.F., Eberhart, R.C., Shi, Y., 2001. Swarm Intelligence. Morgan Kaufmann Publishers, San Francisco.

Kraemer, S.M., Hering, J.G., 1997. Influence of solution saturation state on the kinetics of ligand-controlled dissolution of oxide phases. Geochim. Cosmochim. Acta 61, 2855–2866. doi:10.1016/S0016-7037(97)00133-6.

Lafferty, B.J., Ginder-Vogel, M., Sparks, D.L., 2011. Arsenite oxidation by a poorly-crystalline manganese oxide. 3. Arsenic and manganese desorption. Environ. Sci. Technol. 45, 9218–9223. doi:10.1021/es201281u.

Lafferty, B.J., Ginder-Vogel, M., Sparks, D.L., 2010a. Arsenite oxidation by a poorly crystalline manganese-oxide 1. Stirred-flow experiments. Environ. Sci. Technol. 44, 8460–8466. doi:10.1021/es102013p.

Lafferty, B.J., Ginder-Vogel, M., Zhu, M., Livi, K.J.T., Sparks, D.L., 2010b. Arsenite oxidation by a poorly crystalline manganese-oxide. 2. Results from X-ray absorption spectroscopy and X-ray diffraction. Environ. Sci. Technol. 44, 8467–8472. doi:10.1021/es102016c.

Liu, J., Luo, X., Sun, Y., Tsang, D., Qi, J., Zhang, W., Li, N., Yin, M., Wang, J., Lippold, H., Chen, Y., Sheng, G., 2019. Thallium pollution in China and removal technologies for waters: A review. Environ. Int. 126, 771–790. doi:10.1016/j.envint.2019.01.076.

Manning, B.A., Fendorf, S.E., Bostick, B., Suarez, D.L., 2002. Arsenic(III) oxidation and arsenic(V) adsorption reactions on synthetic birnessite. Environ. Sci. Technol. 36, 976–981. doi:10.1021/es0110170.

Marini, L., Accornero, M., 2007. Prediction of the thermodynamic properties of metal-arsenate and metal-arsenite aqueous complexes to high temperatures and pressures and some geological consequences. Environ. Geol. 52, 1343–1363. doi:10.1007/s00254-006-0578-5.

Moore, J.N., Walker, J.R., Hayes, T.H., 1990. Reaction scheme for the oxidation of As(III) to As(V) by birnessite. Clays Clay Miner 38, 549–555.

Nesbitt, H.W., Canning, G.W., Bancroft, G.M., 1998. XPS study of reductive dissolution of 7Å-birnessite by H_3AsO_3, with constraints on reaction mechanism. Geochim. Cosmochim. Acta 62, 2097–2110. doi:10.1016/S0016-7037(98)00146-X.

Nico, P.S., Zasoski, R.J., 2000. Importance of Mn(III) availability on the rate of Cr(III) oxidation on δ-MnO_2. Environ. Sci. Technol. 34, 3363–3367. doi:10.1021/es991462j.

Oscarson, D.W., Huang, P.M., Liaw, W.K., 1980. The oxidation of arsenite by aquatic sediments. J. Environ. Qual. 9, 700. doi:10.2134/jeq1980.00472425000900040032x.

Parkhurst, D.L., Appelo, C.A.J., 2013. Description of input and examples for PHREEQC version 3—a computer program for speciation, batch-reaction, one-dimensional transport, and inverse geochemical calculations. U.S. Geological Survey Techniques and Methods. USGS.

Peacock, C.L., Sherman, D.M., 2007. Sorption of Ni by birnessite: equilibrium controls on Ni in seawater. Chem. Geol. 238, 94–106. doi:10.1016/j.chemgeo.2006.10.019.

Post, J.E., 1999. Manganese oxide minerals: crystal structures and economic and environmental significance. Proc. Natl. Acad. Sci. 96, 3447–3454. doi:10.1073/pnas.96.7.3447.

Power, L.E., Arai, Y., Sparks, D.L., 2005. Zinc adsorption effects on arsenite oxidation kinetics at the birnessite-water interface. Environ. Sci. Technol. 39, 181–187. doi:10.1021/es049922i.

Prommer, H., Barry, D.A., Zheng, C., 2003. MODFLOW/MT3DMS-based reactive multicomponent transport modeling. Ground Water 41, 247–257. doi:10.1111/j.1745-6584.2003.tb02588.x.

Prommer, H., Sun, J., Helm, L., Rathi, B., Siade, A.J., Morris, R., 2018. Deoxygenation prevents arsenic mobilization during deepwell injection into sulfide-bearing aquifers. Environ. Sci. Technol. 52, 13801–13810. doi:10.1021/acs.est.8b05015.

Prommer, H., Sun, J., Kocar, B.D., 2019. Using reactive transport models to quantify and predict groundwater quality. Elements 15, 87–92. doi:10.2138/gselements.15.2.87.

Qian, A., Zhang, W., Shi, C., Pan .E, C., Giammar, D., Yuan, S., Zhang, H., Wang, Z., 2019. Geochemical stability of dissolved Mn(III) in the presence of pyrophosphate as a model ligand: complexation and disproportionation. Environ. Sci. Technol. 53, 5768–5777. doi:10.1021/acs.est.9b00498.

Ramstedt, M., Andersson, B.M., Shchukarev, A., Sjöberg, S., 2004. Surface properties of hydrous manganite (γ-MnOOH). A potentiometric, electroacoustic, and X-ray photoelectron spectroscopy study. Langmuir 20, 8224–8229. doi:10.1021/la0496338.

Rathi, B., Neidhardt, H., Berg, M., Siade, A.J., Prommer, H., 2017a. Processes governing arsenic retardation on Pleistocene sediments: adsorption experiments and model-based analysis. Water Resour. Res. 53, 4344–4360. doi:10.1002/2017WR020551.

Rathi, B., Siade, A.J., Donn, M.J., Helm, L., Morris, R., Davis, J.A., Berg, M., Prommer, H., 2017b. Multiscale characterization and quantification of arsenic mobilization and attenuation during injection of treated coal seam gas coproduced water into deep aquifers. Water Resour. Res. 53, 10779–10801. doi:10.1002/2017WR021240.

Rawson, J., Siade, A., Sun, J., Neidhardt, H., Berg, M., Prommer, H., 2017. Quantifying reactive transport processes governing arsenic mobility after injection of reactive organic carbon into a Bengal delta aquifer. Environ. Sci. Technol. 51, 8471–8480. doi:10.1021/acs.est.7b02097.

Schacht, L., Ginder-Vogel, M., 2018. Arsenite depletion by manganese oxides: a case study on the limitations of observed first order rate constants. Soil Syst. 2, 39. doi:10.3390/soilsystems2030039.

Scott, M.J., Morgan, J.J., 1995. Reactions at Oxide Surfaces. 1. Oxidation of As(III) by Synthetic Birnessite. Environ. Sci. Technol. 29, 1898–1905. doi:10.1021/es00008a006.

Siade, A.J., Rathi, B., Prommer, H., Welter, D., Doherty, J., 2019. Using heuristic multi-objective optimization for quantifying predictive uncertainty associated with groundwater flow and reactive transport models. J. Hydrol. 577. doi:10.1016/j.jhydrol.2019.123999, 123999.

Simanova, A.A., Kwon, K.D., Bone, S.E., Bargar, J.R., Refson, K., Sposito, G., Peña, J., 2015. Probing the sorption reactivity of the edge surfaces in birnessite nanoparticles using nickel(II). Geochim. Cosmochim. Acta 164, 191–204. doi:10.1016/J.GCA.2015.04.050.

Smedley, P.L., Kinniburgh, D.G., 2002. A review of the source, behaviour and distribution of arsenic in natural waters. Appl. Geochem. 17, 517–568. doi:10.1016/S0883-2927(02)00018-5.

Song, Y., Jiang, J., Ma, J., Zhou, Y., von Gunten, U., 2019. Enhanced transformation of sulfonamide antibiotics by manganese(IV) oxide in the presence of model humic constituents. Water Res. 153, 200–207. doi:10.1016/j.watres.2019.01.011.

Stollenwerk, K., Breit, G.N., Welch, A.H., Yount, J.C., Whitney, J.W., Foster, A.L., Uddin, M.N., Majumder, R.K., Ahmed, N., 2007. Arsenic attenuation by oxidized aquifer sediments in Bangladesh. Sci. Total Environ. 379, 133–150. doi:10.1016/j.scitotenv.2006.11.029.

Stolze, L., Zhang, D., Guo, H., Rolle, M., 2019. Surface complexation modeling of arsenic mobilization from goethite: interpretation of an in-situ experiment. Geochim. Cosmochim. Acta 248, 274–288. doi:10.1016/J.GCA.2019.01.008.

Sun, J., Prommer, H., Siade, A.J., Chillrud, S.N., Mailloux, B.J., Bostick, B.C., 2018. Model-based analysis of arsenic immobilization via iron mineral transformation under advective flows. Environ. Sci. Technol. 52, 9243–9253. doi:10.1021/acs.est.8b01762.

Sverjensky, D.A., 2003. Standard states for the activities of mineral surface sites and species. Geochim. Cosmochim. Acta 67, 17–28. doi:10.1016/S0016-7037(02)01074-8.

Takamatsu, T., Kawashima, M., Koyama, M., 1985. The role of Mn2+-rich hydrous manganese oxide in the accumulation of arsenic in lake sediments. Water Res. 19, 1029–1032. doi:10.1016/0043-1354(85)90372-0.

Tamaki, S., Frankenberger, W.T., 1992. Environmental biochemistry of arsenic. In: Ware, G.W. (Ed.), Reviews of Environmental Contamination and Toxicology. Springer, New York, NY, pp. 79–110. doi:10.1007/978-1-4612-2864-6_4.

Tonkin, J.W., Balistrieri, L.S., Murray, J.W., 2004. Modeling sorption of divalent metal cations on hydrous manganese oxide using the diffuse double layer model. Appl. Geochem. 19, 29–53. doi:10.1016/S0883-2927(03)00115-X.

Tournassat, C., Charlet, L., Bosbach, D., Manceau, A., 2002. Arsenic(III) oxidation by birnessite and precipitation of manganese(II) arsenate. Environ. Sci. Technol. 36, 493–500. doi:10.1021/es0109500.

Villalobos, M., 2015. The role of surface edge sites in metal(loid) sorption to poorly-crystalline birnessites, in: advances in the environmental biogeochemistry of manganese oxides. Am. Chem. Soc. 65–87. doi:10.1021/bk-2015-1197.ch00410.1021/bk-2015-1197.ch004.

Villalobos, M., Escobar-Quiroz, I.N., Salazar-Camacho, C., 2014. The influence of particle size and structure on the sorption and oxidation behavior of birnessite: I. Adsorption of As(V) and oxidation of As(III). Geochim. Cosmochim. Acta 125, 564–581. doi:10.1016/j.gca.2013.10.029.

Villalobos, M., Toner, B., Bargar, J., Sposito, G., 2003. Characterization of the manganese oxide produced by pseudomonas putida strain MnB1. Geochim. Cosmochim. Acta 67, 2649–2662. doi:10.1016/S0016-7037(03)00217-5.

Wallis, I., Prommer, H., Simmons, C.T., Post, V., Stuyfzand, P.J., 2010. Evaluation of conceptual and numerical models for arsenic mobilization and attenuation during managed aquifer recharge. Environ. Sci. Technol. 44, 5035–5041. doi:10.1021/es100463q.

Wang, Q., Yang, P., Zhu, M., 2019. Effects of metal cations on coupled birnessite structural transformation and natural organic matter adsorption and oxidation. Geochim. Cosmochim. Acta 250, 292–310. doi:10.1016/j.gca.2019.01.035.

Wang, Q., Yang, P., Zhu, M., 2018. Structural transformation of birnessite by fulvic acid under anoxic conditions. Environ. Sci. Technol. 52, 1844–1853. doi:10.1021/acs.est.7b04379.

Wang, Z., Giammar, D.E., 2013. Mass action expressions for bidentate adsorption in surface complexation modeling: theory and practice. Environ. Sci. Technol. 47, 3982–3996. doi:10.1021/es305180e.

Wang, Z., Lee, S.-.W., Catalano, J.G., Lezama-Pacheco, J.S., Bargar, J.R., Tebo, B.M., Giammar, D.E., 2013. Adsorption of uranium(VI) to manganese oxides: X-ray absorption spectroscopy and surface complexation modeling. Environ. Sci. Technol. 47, 850–858. doi:10.1021/es304454g.

Wu, Y., Li, W., Sparks, D.L., 2015. The effects of iron(II) on the kinetics of arsenic oxidation and sorption on manganese oxides. J. Colloid Interface Sci. 457, 319–328. doi:10.1016/j.jcis.2015.07.022.

Yang, P., E. Post, J., Wang, Q., Xu, W., Geiss, R., R. McCurdy, P., Zhu, M., 2019. Metal adsorption controls stability of layered manganese oxides. Environ. Sci. Technol. 53, 7453–7462. doi:10.1021/acs.est.9b01242.

Yao, W., Millero, F.J., 1996. Adsorption of phosphate on manganese dioxide in seawater. Environ. Sci. Technol. 30, 536–541. doi:10.1021/es950290x.

Ying, S.C., Kocar, B.D., Griffis, S.D., Fendorf, S., 2011. Competitive microbially and Mn oxide mediated redox processes controlling arsenic speciation and partitioning. Environ. Sci. Technol. 45, 5572–5579. doi:10.1021/es200351m.

Zhao, H., Zhu, M., Li, W., Elzinga, E.J., Villalobos, M., Liu, F., Zhang, J., Feng, X., Sparks, D.L., 2016. Redox reactions between Mn(II) and hexagonal birnessite change its layer symmetry. Environ. Sci. Technol. 50, 1750–1758. doi:10.1021/acs.est.5b04436.

Zhu, M., Paul, K.W., Kubicki, J.D., Sparks, D.L., 2009. Quantum chemical study of arsenic (III, V) adsorption on Mn-oxides: implications for arsenic(III) oxidation. Environ. Sci. Technol. 43, 6655–6661. doi:10.1021/es900537e.